



**University of
Sunderland**

Zubairuddin, Mohammed, Pradeep, G. V. Krishna, Shaikh, Javed Habib, Joshi, Gaurang, Darji, Raghavendra and Mohan, Dhanesh G. (2025) Predictive Modeling of Activated Tungsten Inert Gas Welding in Grade 91 Steel Using Finite Element Method and Experimental Techniques. *steel research international*. p. 2500072. ISSN 1869-344X

Downloaded from: <http://sure.sunderland.ac.uk/id/eprint/18995/>

Usage guidelines

Please refer to the usage guidelines at <http://sure.sunderland.ac.uk/policies.html> or alternatively contact

sure@sunderland.ac.uk.

Predictive Modeling of Activated Tungsten Inert Gas Welding in Grade 91 Steel Using Finite Element Method and Experimental Techniques

Mohammed Zubairuddin, G. V. Krishna Pradeep, Javed Habib Shaikh, Gaurang Joshi, Raghavendra Darji, and Dhanesh G. Mohan*

Grade 91 steel, a ferritic-martensitic alloy, is commonly used in thermal power and nuclear plants due to its high-temperature, high-pressure performance. This study analyzes the thermal and mechanical behaviour of activated tungsten inert gas (A-TIG) welding on 4 mm-thick Grade 91 steel using an in-house developed oxide flux. Transient temperatures are recorded at multiple locations during welding. X-ray diffraction is used to evaluate residual stress, with peak tensile stress near the heat-affected zone reaching 471 MPa. The A-TIG process yields deep penetration and narrow weld beads due to high heat intensity. A finite element simulation incorporating a combined heat source model (conical and double ellipsoidal) is used to predict temperature, stress, and distortion. Longitudinal distortion predictions are compared with experimental results, showing good agreement. Distortion analysis using various theories confirms the accuracy of the simulation. Phase transformations from ferrite to austenite and then to martensite are included in the model, enhancing prediction accuracy. The combined model with large deformation and phase transformation effects provides results closely matching experimental data for both thermal and mechanical responses.

nuclear reactors. Grade 91 steel received strong carbide- and nitride-forming elements, such as V and Nb, with small N additions for extending its high-temperature creep strength at long durations. Grade 91 steel maintains excellent weldability, high thermal expansion coefficient properties, high corrosion resistance and toughness, and high thermal conductivity and ductility under high-temperature conditions. Grade 91 steels serve as tubing materials in nuclear and thermal power plants to temperatures up to 600 °C. Grade 91 steel can be welded using different welding processes like manual metal arc welding, shielded arc welding, laser, electron beam, and tungsten inert gas (TIG) or gas tungsten arc (GTA) welding process. GTA or welding is considered superior to other types of welding because the applied molten metal is protected from the atmosphere using inert gas.^[1–7] It is commonly preferred for thin plate welding

and for thick plate, the multipass welding technique is used. In multipass welding, TIG welding process is used for root-pass welding.

1. Introduction

Grade 91 creep strength enhanced ferritic steels are superheater headers and tubes in ultra-supercritical power plants and

M. Zubairuddin, G. V. K. Pradeep
Department of Mechanical Engineering
Aditya University
Surampalem, Kakinada, Andhra Pradesh 533437, India

J. H. Shaikh
Department of Mechanical Engineering
M.H. Saboo Siddik College of Engineering
Mumbai 400008, India

G. Joshi
Department of Mechanical Engineering
Marwadi University
Rajkot 360003, India

 The ORCID identification number(s) for the author(s) of this article can be found under <https://doi.org/10.1002/srin.202500072>.

© 2025 The Author(s). Steel Research International published by Wiley-VCH GmbH. This is an open access article under the terms of the Creative Commons Attribution License, which permits use, distribution and reproduction in any medium, provided the original work is properly cited.

DOI: 10.1002/srin.202500072

R. Darji
Materials Engineering
Matter Motor Works Pvt. Ltd.
DCT – Khodiyar, Ahmedabad 382475, India

D. G. Mohan
School of Computer Science and Engineering
University of Sunderland
Sunderland SR6 0DD, UK
E-mail: dhanesh.mohan@sunderland.ac.uk

D. G. Mohan
Centre of Research Impact and Outcome
Chitkara University Institute of Engineering and Technology
Chitkara University
Rajpura, Punjab 140401, India

The main drawbacks of TIG welding include the constraint on welding thickness, difficulties in welding various material compositions simultaneously, and reduced productivity figures. Single-pass welding operations have a maximum thickness limit, while the material composition variance (cast to cast) shows poor tolerance during TIG welding and low productivity. Weld penetration reaches its maximum depth during single-pass TIG steel welds though TIG welding must be 3 mm or less when protected by argon shielding gas. Joint penetration during welding varies because different heats of material show small fluctuations in chemical content. Steel weld penetration remains variable during weld operations, especially in autogenous TIG welds or the root pass of multiple-pass TIG welds. A poor combination of slow welding speeds with in-speeds determines TIG welding productivity. The joint filling process requires many welding passes due to the thickness of the material. Over the years, various strategies have emerged as solutions to enhance either weld penetration depth or production efficiency of the TIG process. Industry experts have discovered that applying arc penetration coatings will produce robust results in TIG welding applications. Flux coating on the joined surfaces improves welding penetration. It is observed that mechanical behavior is enhanced in the case of 304 L, 316 L, and P91 steel using the activated TIG (A-TIG) welding process.^[8–11]

Arunkumar et al. critically observed the A-TIG welding of P91 steel. The flux coating effect on penetration was studied. The author discussed that the usage of flux dramatically enhanced the weld penetration. Comparison with the TIG process showed that the high tensile strength of the weldment is observed in flux-coated plates.^[9] Maduraimuthu et al. examined the P91 steel and its optimization. It was observed from the results that the A-TIG plates have higher hardness, yield strength, and ultimate tensile strength values in comparison with the TIG-welded joints. The toughness value was lower than that of the TIG-welded joints because of the ferrite phase formation in the A-TIG process. Residual stress was observed as tensile in the TIG process, whereas in A-TIG welding, it was compressive.^[10] Vasudevan et al. studied the principles of optimizing the A-TIG process. Input values: voltage, current, and weld speed. The response was plotted as weld penetration, width, and heat affected zone. The optimization technique that was applied in this work is known as the genetic algorithm (GA). The study has shown that the shape and width of the HAZ were calculated through the experimental values of the optimized process parameters achieved using the multiobjective GA optimization, which was well within an acceptable range.^[11] Arivazhagen et al. performed the A-TIG experiments on P91 steel. Based on the results, the essence of the hardness is the magnetism of solidification of A-TIG weld joints containing a higher concentration of carbon than standard TIG weld joints. As a result, the study's results indicated that the hardness value was lower in the case of the A-TIG process than after postweld heat treatment.^[12] Nagaraju et al. optimized the A-TIG for P91 material and discussed the response surface methodology technique.^[13] Pandey et al. discussed the hydrogen assistance cracking (HAC) phenomena, P91 is subjected to HAC, and it transformed to unwanted martensitic metallurgical transformation in the HAZ. In another paper, the author also discussed the effect of diffusible hydrogen content on lower critical stress, flexural strength, and tensile

strength.^[14,15] Taraphdar et al. discussed the effect of different weld grooves in 40 mm-thick multipass high-strength steel on the residual stresses.^[16]

The finite element analysis (FEA) technique helps to predict distortion and stress before actual welding. The literature shows that SYSWELD, ABAQUS, and ANSYS software are famous for studying the thermal and mechanical behavior of P91 steel welding.^[14–20] M. Zubairuddin et al. discussed the thermal, metallurgy, and mechanical simulation of P91 steel for 2–3 mm plate welded by autogenous welding and 6 mm-thick multipass welding, considering the preheating welded by the laser and GTA welding process.^[18–21] S Kumar et al. validated FEM-based predicted stresses in different directions of P91 material joined by the laser process.^[18] Yaghi et al. calculated the stress of P91 steel pipes using ABAQUS and further compared with FEM-based predicted results.^[22] Kim et al. calculated stress without considering the phase transformation using the FEM method for P91 steel.^[23]

Ganesh et al. discussed the FEM-based analysis of a 3 mm-thick 316LN material in the SYSWELD and ANSYS software.^[24,25] Pavan et al. studied the 2.25 Cr-1Mo steel plate welding analysis and predicted result of distortion and residual stress validated with experimental results.^[26,27] Based on the literature survey, it is observed that mechanical and metallurgical studies have been carried out but limited work is available in the FEA of the A-TIG welding process for P91 steel. This article discussed the FEM-based analysis of A-TIG welding of Grade 91 steel and its experimental validation of thermal history, distortion, and stress in a 4 mm-thick plate.

2. Experimental Section

In this investigation, Grade 91 steel was fabricated by employing TIG welding. The TIG welding was carried out on thin sheets of Grade 91 steel plate with 300 × 250 × 4 mm dimensions. For the test blanket module trial in the upcoming (ITER) fusion reactor, Grade 91 material will be used as a surrogating material with a 4–10 mm-thick plate. Activating flux was prepared by weighing the appropriate quantity of flux in a beaker, which was dried in the furnace for a while. Then, the activating flux paste was made by mixing with acetone to coat the welding surface. Before welding, the plate was cleaned with acetone for moisture removal. The activating flux paste was then applied to the welding surface using a paintbrush and allowed to dry, leaving a flux coating on the welding surface. Autogenous welding was carried out after the flux was dried. K-type thermocouples were spot welded on the weld plate at a 15–10 mm distance from the weld line for temperature measurement. **Figure 1** and **2** shows the bead-on-plate welding of Grade 91 steel plate for the A-TIG and TIG process.

Welding parameters were selected based on the initial bead-on-plate trial which ensured the full penetration depth for all cases. Two bead-on-plate experiments were performed for the A-TIG process to ensure a minimum amount of weld width. Further, the same optimum heat input values were given to the square butt joint plate welded by A-TIG process. For studying the effect of heat input in the TIG and A-TIG welding process, at the same heat input, another bead-on-plate experiment

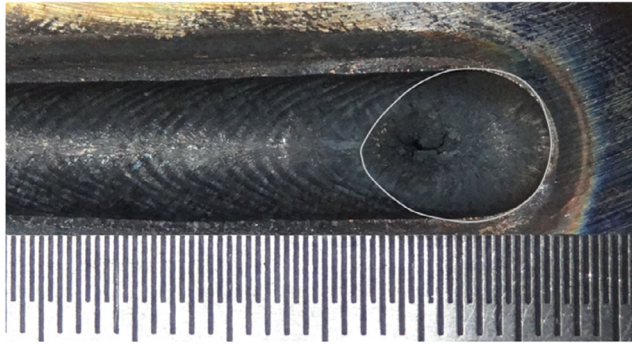
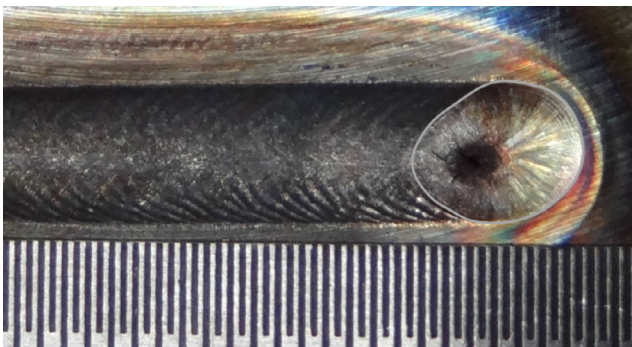


Figure 1. Bead on a plate of TIG welding.

(a)



(b)

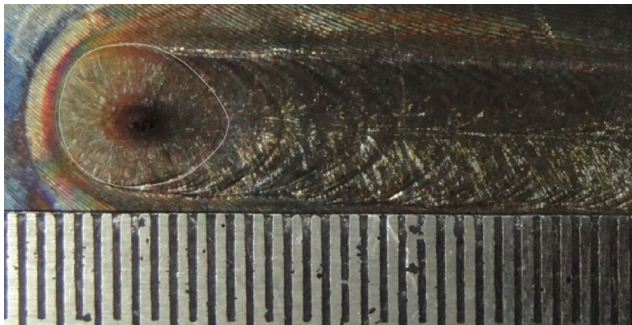


Figure 2. Bead on plate. a) Plate number 1. b) Plate number 2.

was conducted for the TIG welding process. The square butt joint plate experimental setup for the A-TIG welding process is shown in Figure 1. Heat input values for both processes are shown in Table 1 and 2.

Residual stresses produced in weld plates were measured using the $\sin^2\psi$ method in X-ray diffraction (XRD). The peak in diffraction was first found with peak fitting techniques, Lorentz-polarization-absorption corrections, and proper background subtraction. Bragg's law was used for measuring the d space with predefined n set (1), measured diffraction angle (2θ), and X-ray wavelength (λ).^[13] Distortion in weld plate was measured on grid mark position using electronic Vernier height gauge. The experimental setup of A-TIG square butt joint plate is shown (Figure 3).

Table 1. Heat input parameters for TIG welding.

Current [A]	Voltage [V]	Weld Speed [mm min ⁻¹]	Arc Gap [mm]	Gas Flow Rate [l min ⁻¹]	Electrode Angle [degree]	Heat Input [J mm ⁻¹]
110	12	100	3	10	30	790

Table 2. Heat input parameters for a-TIG welding.

Current [A]	Voltage [V]	Weld Speed [mm min ⁻¹]	Arc Gap [mm]	Gas Flow Rate [l min ⁻¹]	Electrode Angle [degree]	Heat Input [J mm ⁻¹]
115	12	100	3	10	30	826
110	12	100	3	10	30	790



Figure 3. Experimental setup of A-TIG square butt joint plate with Ver.

3. Modeling and Heat Equation

Heat input is the major factor for the application of the thermal cycle on weld plates. The following equation gives the heat input.

$$Q = \frac{V \cdot I}{v \cdot 1000} \text{ kJ/mm} \quad (1)$$

V = Voltage (V)

v = Velocity (mm s⁻¹)

I = Current (A)

Q = Heat input (kJ mm⁻¹)

3.1. Heat Transfer

The heat distribution due to arc welding has been successfully modeled using a double ellipsoidal configuration. It is fascinating to note that the heat is distributed through conduction and convection to the surroundings plays an important role.

Heat transfer in welding depends on several parameters, like the geometry of the plate, material properties, atmospheric condition, and so on. Conduction in weld plates is explained with the 3D heat transfer equation.^[18]

$$\frac{\partial k \partial T / \partial x}{\partial x} + \frac{\partial k \partial T / \partial y}{\partial y} + \frac{\partial k \partial T / \partial z}{\partial z} + Q = \rho C_p \frac{\partial T}{\partial t} \quad (2)$$

The natural boundary condition can be defined as

$$k_n \frac{\partial T}{\partial n} + q + \alpha(T(x, y, z, t) - T_a) + \sigma \epsilon(T(x, y, z, t)^4 - T_a^4) = 0 \quad (3)$$

where, (x, y, z) are points on the boundary for times after $t = 0$.

α = Heat transfer coefficient ($\text{W m}^{-2} \text{ } ^\circ\text{C}$)

k_n = Thermal conductivity ($\text{W m}^{-1} \text{ } ^\circ\text{C}$)

T_a = Atmospheric condition ($^\circ\text{C}$)

$q(x, y, z, t)$ = Heat flux (W m^{-2})

3.2. Heat Source Considering the Double Ellipsoidal Model

Heat power density (W m^{-3}) in Gaussian distribution is considered with its center at $(0, 0, 0)$.^[28,29]

The heat power distribution is

$$q_f(x, y, z, t) = \frac{6\sqrt{3}f_r Q}{a_f b c \pi \sqrt{\pi}} e^{-3x^2/a_f^2} e^{-3y^2/b^2} e^{-3[z+v(\tau-t)]^2/c_1^2} \quad (4)$$

$$q_r(x, y, z, t) = \frac{6\sqrt{3}f_r Q}{a_r b c \pi \sqrt{\pi}} e^{-3x^2/a_r^2} e^{-3y^2/b^2} e^{-3[z+v(\tau-t)]^2/c_1^2} \quad (5)$$

In the double-ellipsoidal model, the heat source parameters are set as follows

$c = 4 \text{ mm}$ (vertical axis)

$a_r = 7.5 \text{ mm}$ (rear axis)

$a_f = 2.5 \text{ mm}$ (front axis)

$b = 7 \text{ mm}$

The above values help to predict the size and shape of the heat source model. Weld speed is reported to be 1.67 mm s^{-1} , where

' f ' represents the heat deposition fraction in rear and front quadrants, where $f_r + f_f = 2$. The difference in ellipsoid size is obtained using ' c_2 ' and ' c_1 ' as the semiaxes behind and ahead.

3.3. Heat Source Considering the Conical Model

In FEM-based analysis, the reassurance of the heat being observed at the top is further followed by a gradual reduction in a conical shape from high to low in thickness. This gradual decrease in heat is essential for the conical model, which ensures high penetration, as mentioned in the literature. **Figure 4b** illustrates the 3D conical model popular for high-density processes.

Heat supplied is given as^[20]

$$Q = Q_0 e^{\left(\frac{-3r^2}{r_0^2}\right)} \quad (6)$$

$$r = \sqrt{x^2 + y^2} \quad (7)$$

$$r_0 = r_e - \left[\frac{(r_e - r_i)(z_e - z)}{(z_e - z_i)} \right] \quad (8)$$

Parameters for the heat source model are r_i and r_e radii in the plane directions Z_i and Z_e .

3.4. Combined Double-Ellipsoidal and Conical Model

High-energy weld bead cross section shows an elliptical upper portion like a nail head. A Goldak's model is attached to a 3D conical heat source to account for that nail head shape. The power for each heat source is then distributed according to HSF as $60 + 40\%$ of heat input, as shown in **Figure 5**.

4. Meshing and Boundary Condition

Heating is done along all the elements and can be prolonged to include the whole construction. There is also another way of describing the weld path using trajectory and reference line, more so the start and want and node of the start element as

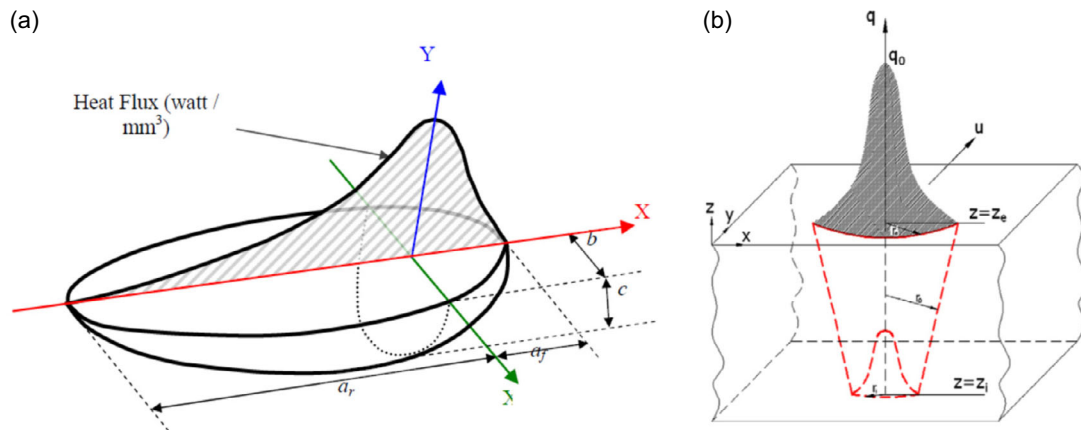


Figure 4. Heat source models. a) Double-ellipsoidal model. b) 3D conical model.

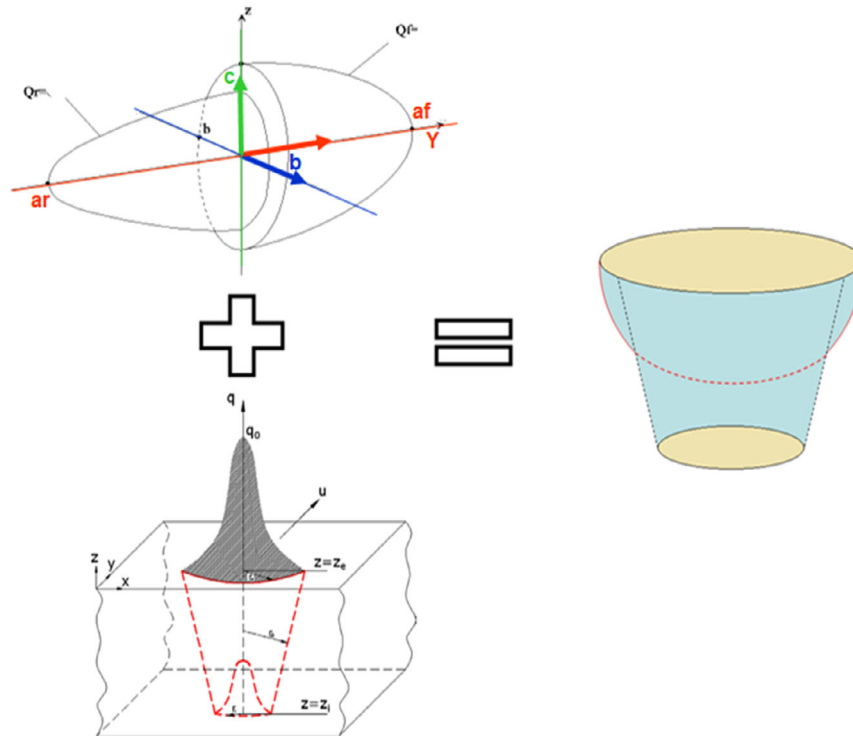


Figure 5. 3D conical Gaussian with cylindrical Gaussian heat source.

shown in **Figure 6**. A trajectory line contains all the information on the definition of the motion of weld source space and the path of the center of power source, which is equivalent to the local Y-axis, parallel to the weld line element. This line is applied on the skin of the joint and not in the root. The reference line is a 1D element as shown in Figure 6a,b and is parallel with the weld line. It is used similarly to the weld line to specify the standard trajectory and must comprise as many pieces as the weld line. The parameters that should be entered into this group do not differ from the parameters of trajectory, which are the start node, the end node, and the start element. If no reference data are to be specified, the source must be axially symmetrical relative to the trajectory. Once more, the start node is just one node that defines the place of the start-point of the trajectory.

Visual Mesh is a SYSWELD software module used for meshing and modeling. The meshing of square butt plate of size $300 \times 125 \times 4$ mm and bead-on-plate of size $60 \times 100 \times 4$ mm is observed in Figure 6a,b. The number of nodes and solid elements for the square plate are 188 689 and 67 321, respectively. In HAZ and fusion zone (FZ) area, size of the element is kept at $0.5 \times 0.5 \times 0.5$ mm. The size of meshing is increased from FZ to base metal.

The following assumptions are made in the model formulation during FEA of weld. 1) The initial temperature of the plate and atmospheric temperature is considered as 26°C . For welding with a heating case, initial and atmospheric temperature of the plate is considered as 200°C . 2) Material properties are homogenous, isotropic, and temperature dependent. 3) The welding heat source moves at a certain predefined speed in the welding direction on the weld trajectory only. 4) The present analysis balanced the convection stirring in the molten pool by artificially

doubling the material's thermal conductivity after the melting point.

The temperature distributions obtained by solving the heat conduction equation from thermal analysis will be further used as input for mechanical analysis to obtain stress-strain fields. The mechanical analysis is based on the solution of force equilibrium equations. The elastic strain component is modeled using isotropic Hook's law with temperature-dependent Young's modulus and Poisson's ratio. The plastic behavior is employed with the von Mises criterion, temperature-dependent mechanical properties, and isotropic hardening model. To calculate the thermometallurgical strain, strains arising from temperature-dependent thermal expansion coefficient and phase change are included. Movement of the weld plate is restricted by clamping the weld plate at the three different corners in different directions, as shown in Figure 6b.

5. Result and Discussion

A-TIG affects the shape and size of FZ, HAZ, and boundaries. Initially, heat source fitting (HSF) was modeled for complete penetration at the optimum heat input parameters. Thermomechanical modeling of the bead on the plate was calculated considering double-ellipsoidal and combined conical and double-ellipsoidal models.

5.1. HSF

The weld profile was calculated using the HSF analysis, the input model parameters were measured from the weld crater

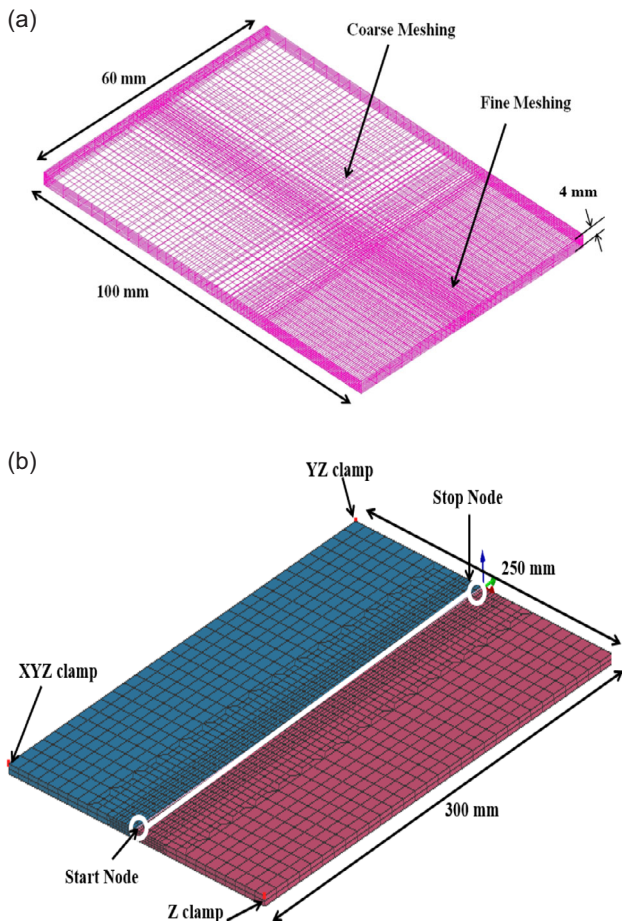


Figure 6. Meshing and clamping. a) Bead on plate. b) Square butt joint plate.

as shown in Figure 1 and 2. At different heat inputs, weld profile is observed in **Figure 7** and **8** for TIG and A-TIG processes. The experimentally measured size of the FZ in TIG welding is 8.5 mm. In the case of the A-TIG bead on plate-1, the FZ is reduced up to 8.35 mm only and for the bead on plate-2, it is reduced more significantly up to 6.72 mm. HAZ size in TIG welding is observed at 17.3 mm, it is reduced to 15.1 (bead on plate-1) and 12.9 mm (bead on plate-2) in A-TIG welding. Based on the comparison it is observed that the bead on plate-2 has less HAZ and FZ size.

For the TIG weld joint, grain size of the weld metal was 92–100 μm , and for the A-TIG weld joint, the grain size of the weld metal was 100–110 μm , as shown in **Figure 9**.

Based on literature and previous experimental work, it is observed that for TIG and laser welding, the double-ellipsoidal model and conical model showed a good prediction in the case of the P91 steel weld.^[18–20] In the case of A-TIG weld analysis, it is observed that the weld profile is closer by combining the conical and double-ellipsoidal models. The double ellipsoidal model gives wider weld width at the top of the plate and narrow at the bottom with less penetration, whereas, the conical model represents deeper penetration. While combining both models, it is observed that there is a reduction in weld width at the top with



Figure 7. TIG welding bead on plate.

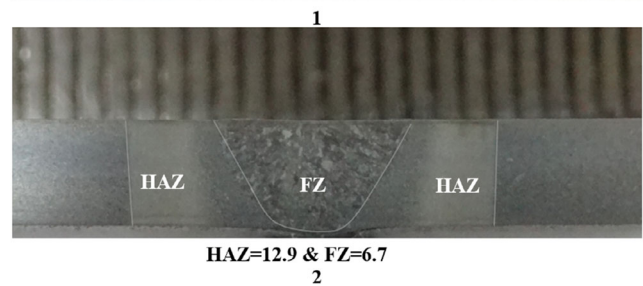


Figure 8. Weld profile of A-TIG welding bead on a plate (Two cases).

full depth of penetration, which is closer to the experimental profile. The predicted weld profile of TIG and A-TIG welding for both the bead on the plate is shown in **Figure 10**. Predicted HAZ in the case of TIG welding is 18 mm, which is more than A-TIG case 12.4 mm (for bead on plate-2) and 15.8 mm (for bead on plate-1). The predicted FZ size in TIG welding is 9.3 mm and in the case of A-TIG is 7.2 mm (For bead on plate-2). In both FZ and HAZ profiles, shaper and values are approximately nearer to experimentally measured values.

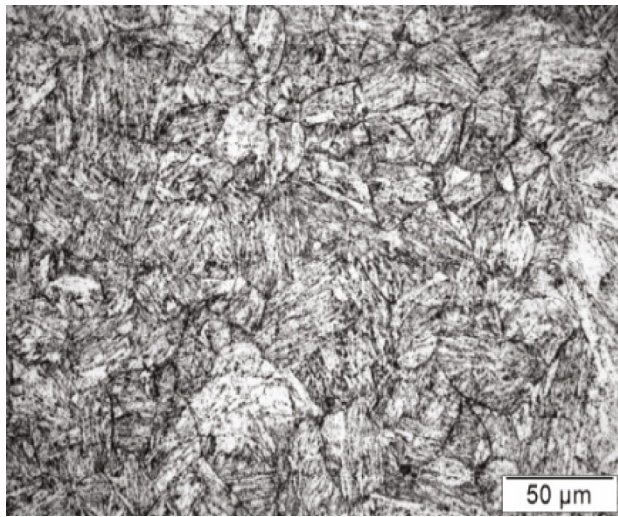
5.2. Thermal Analysis

FEM-based thermal simulation shows that the maximum temperature value is 1645 $^{\circ}\text{C}$ (1510 $^{\circ}\text{C}$ melting point), observed with pink color as shown in **Figure 11**. In thermal analysis, it is noted that due to Goldak's model with double-ellipsoidal consideration, the top of weld plate shows broad FZ as compared to the bottom because conical model thickness of FZ is constant nearer to the bottom.

Predicted thermal cycles at 15 and 10 mm distance from the weld center are validated with experimental values, as shown in **Figure 12** and **13**. The FEM-based-calculated maximum temperature is 659 $^{\circ}\text{C}$ observed at a 10 mm distance. This is close to experimental values of 621 $^{\circ}\text{C}$. At a 15 mm distance, the maximum predicted temperature value is 438 $^{\circ}\text{C}$ and experimental value at the exact location is 418 $^{\circ}\text{C}$. In both the thermal cycle comparisons, as shown in Figure 12 and 13, it is observed that predicted thermal cycles follow the same pattern during heating and cooling with experimentally recorded thermal history at two different locations, it shows the accuracy of the combined heat source model.



1. TIG welding



2. A-TIG

Figure 9. Microstructure of TIG and A-TIG at weld zone.

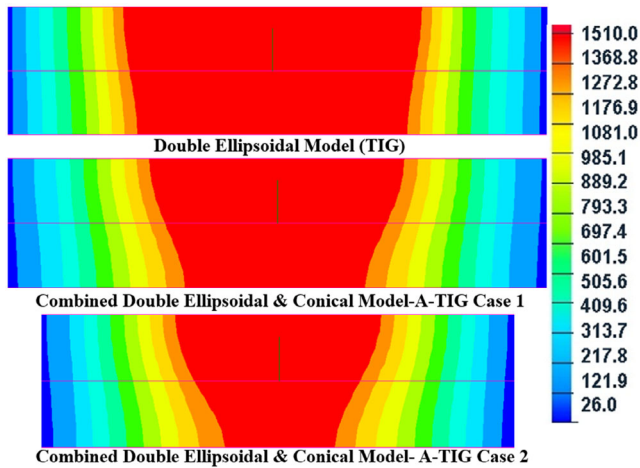


Figure 10. HSG for TIG and A-TIG bead on plate.

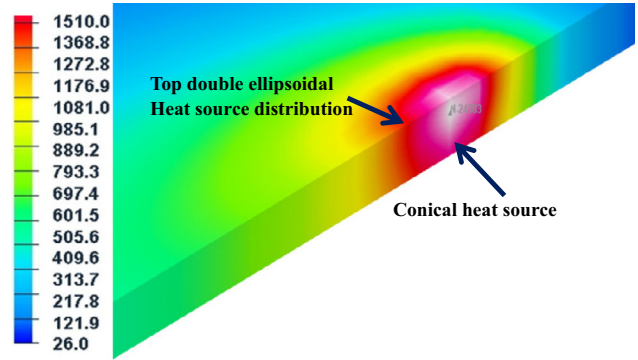


Figure 11. Thermal analysis of A-TIG (considering the combined model).

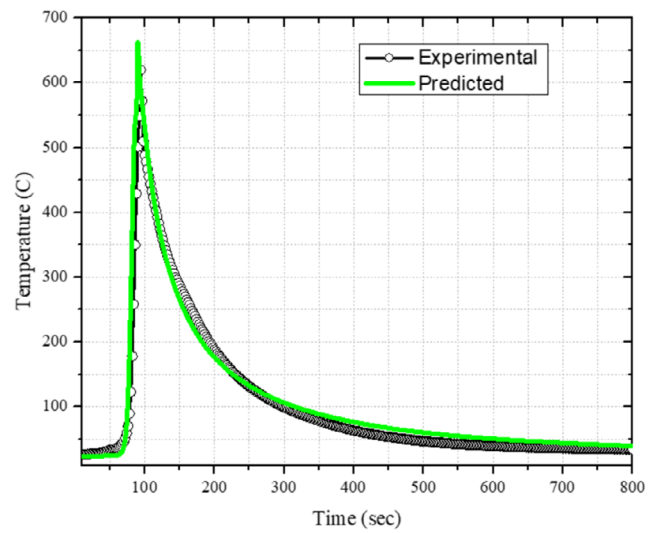


Figure 12. Thermal cycle comparison for A-TIG at 10 mm distance weld line.

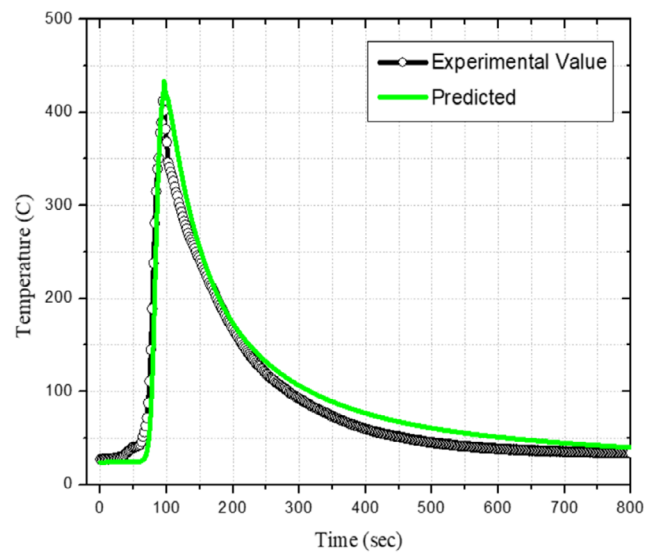


Figure 13. Thermal cycle comparison for A-TIG welding at 15 mm distance.

5.3. Stress Analysis

During the cooling of weld plates, thermal and plastic deformation occur which causes further generation of residual stresses. Grade 91 creep-enhanced steel is ferritic–martensitic steel, which has a ferrite phase at the initial weld condition, during the welding it

changes to austenite and after welding it changes to martensitic with an increase in volume.^[16] Stresses in weld plates were calculated using the XRD method at an interval of 5 mm in the transverse direction. **Figure 14** compares the predicted and measured stress values. The effect of phase transformation is observed at the weld line (FZ) with high-stress value due to the martensitic phase with body centered tetragonal structure, while away from FZ, the phase is ferrite with body centered cubic structure that has less stress value. Different authors reported a similar stress profile (M Profile) for TIG, MMAW, and laser welding for P91 steel.^[1–4]

Experimentally measured stress profile shows that the tensile stress value at the HAZ gradually transfers into compressive stress. It is noted that the maximum stress value is 491 MPa, next to HAZ at a 15 mm distance from the center line. Toward the corner of the plates, the stress is compressive. Figure 14 compares predicted and experimentally observed residual stress in A-TIG weld joints, showing a high degree of agreement. The material phase transformation and shrinkage of molten metal during the solidification induced the peak residual tensile stress close to the interface of the weld and HAZ. In the case of simulation, the maximum stress value is 542 MPa. The effect of phase transformation is observed in the stress profile from minimum stress value at the weld line to maximum next to HAZ. The compressive stress value is observed for predicted and measured values for A-TIG welding, it is reaching up to -240 MPa.

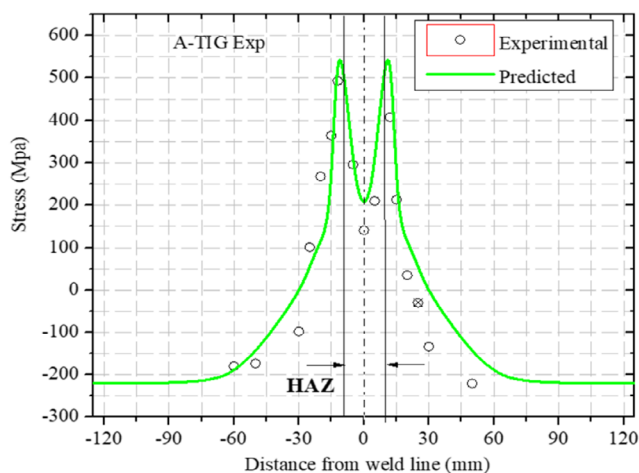


Figure 14. Residual stress comparison.

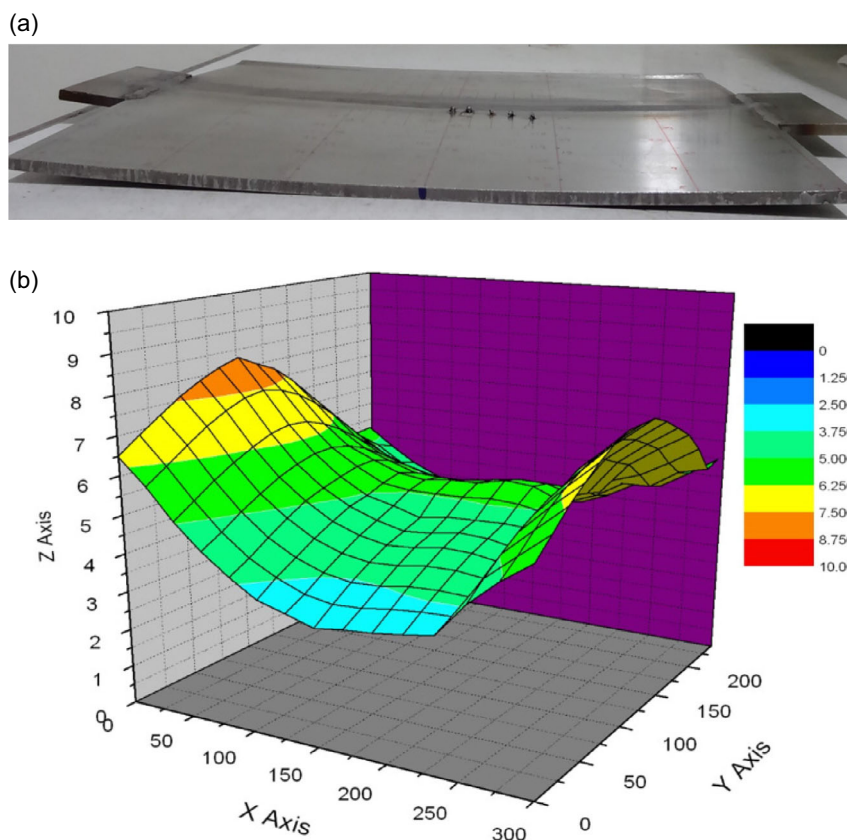


Figure 15. Distortion in weld plate. a) Distortion in actual weld plate and b) experimentally measured distortion.

H.T. ADVISOR

DISPLACEMENTS_NOD_Z(L1)
min=-1.6 at NODE 37759 in TRIAL-3_V_POST2000.tdb
max=3.3 at NODE 71109 in TRIAL-3_V_POST2000.tdb

17 / 3500.000000

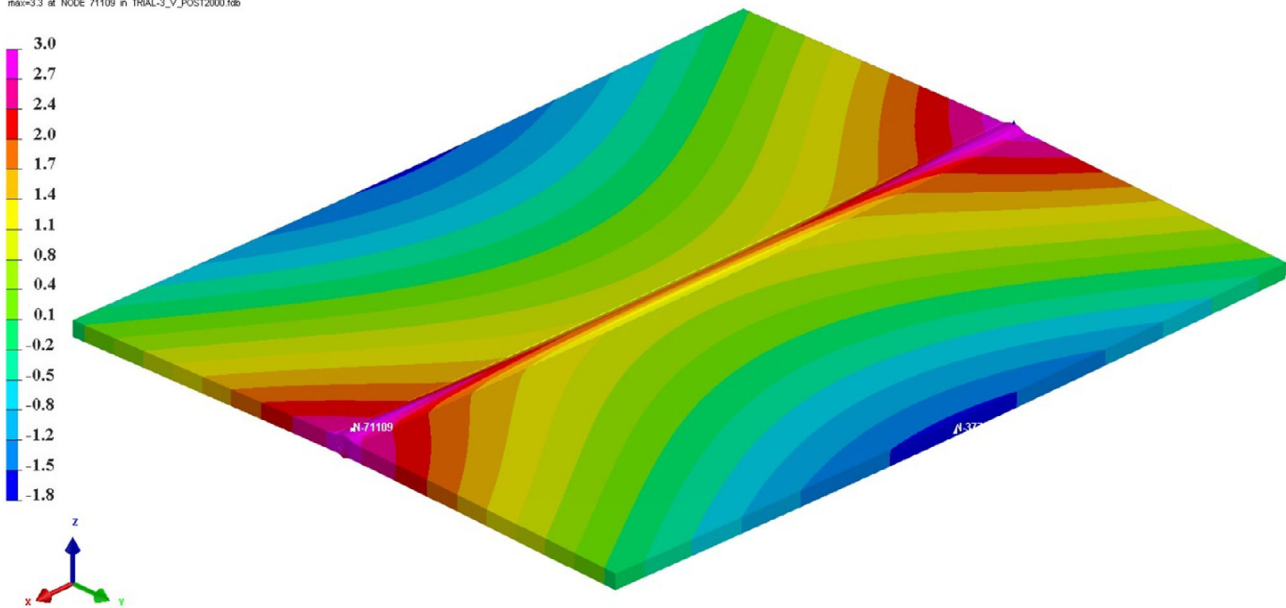


Figure 16. Predicted distortion in weld plate.

5.4. Distortion Analysis

During the welding process, heating and cooling the plate cause expansion and contraction, inducing stresses in the plate. These residual stresses exceed the yield value and cause plastic deformation in the form of distortion in the weld plate. Heat input affects both the stress and the distortion in the weld plate. Higher heat input produces a wider HAZ and a more significant temperature gradient, which increases the thermal stresses and the potential for distortion. After releasing the weld clamp, plates were bowed up, releasing the residual stresses. **Figure 15a** shows the out-of-plane distortion in the weld plate. Based on the grid marking on the weld plate, the difference between before and after welding distortion in the plate is measured and plotted as shown in **Figure 15b**.

Three different cases have been considered in FEM-based distortion analysis. In the first case, the large distortion theory has been considered in the analysis with a linear relation between strain and displacement. In the second case, distortion analysis was calculated using small distortion theory considering the non-linear relations between strains. For studying the phase transformation effect in A-TIG welding, in the last case, the phase transformation has been removed from the material by using only one phase property in the database and distortion is predicted using large distortion theory only. Predicted distortion in the square butt joint plate for the A-TIG welding process is shown in **Figure 16**. The predicted distortion profile exhibits a significant buckling mode of distortion in all cases due to similar types of clamping considerations. In the boundary condition, the clamping force was considered at different three corners. The sequence of unclamping was not considered in the analysis.

FEM-based calculated weld distortion in the longitudinal direction is validated with recorded values as shown in **Figure 17**. The numerically predicted distortion profile looks more like the

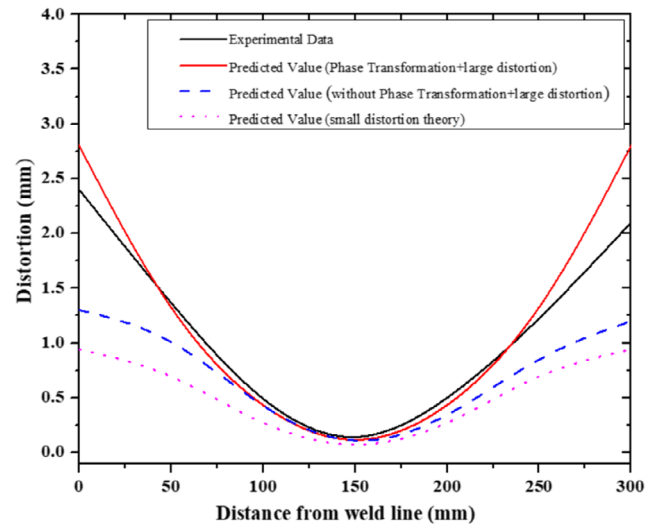


Figure 17. Comparison of predicted and experimental distortion.

experimental distortion profile. Maximum displacement is produced at the left corner with a value of 2.43 mm, at the same location predicted value is 2.78 mm for case-1 distortion analysis. For the second case, it shows 1.25 mm and for the case third, it is reduced up to 0.94 mm. For only case 1, distortion analysis shows a good agreement with the measured one.

6. Conclusion

Using two different heat source models, the HSF analyses of conventional TIG and A-TIG processes were compared for P91 steel

plates. The results comparison showed the FEM model predicted a reasonable prediction of distortion, stress, and thermal cycles.

However, some important conclusions are listed below. 1) A comparison of TIG and A-TIG welding showed a full-depth penetration at 792 and 659 J mm⁻¹ heat input, respectively. 2) Predicted and measured maximum temperature values at 10 and 15 mm are 498 °C and 418 °C for A-TIG welding, respectively, predicted results at the same place show only 5–6 errors. 3) Maximum predicted stress value is 542 MPa with an error of 10%, whereas, the measured stress value is 491 MPa with tensile nature for A-TIG welding. 4) Phase transformation is observed in both predicted and calculated stress profiles. 5) Distortions in the longitudinal direction were compared for predicted and experimental results. Three different simulations were compared for different conditions. Phase transformation with large distortion theory predicted distortion with an error of 5% only. Consideration of small distortion theory shows an error of 55% and without transformation the error was 49%. Hence, effect of phase transformation is dominating in the case of A-TIG welding of Grade 91 steel.

Acknowledgements

The authors gratefully acknowledge the staff and laboratory members from Aditya University, Surampalem, India; M.H. Saboo Siddik College of Engineering, Mumbai, India; Marwadi University, Rajkot, India; the Materials Engineering team at Matter Motor Works Pvt. Ltd., Ahmedabad, India; the University of Sunderland, Sunderland, United Kingdom; and Chitkara University, Punjab, India for their valuable and immersive support throughout the course of this work.

Conflict of Interest

The authors declare no conflict of interest.

Data Availability Statement

All the data related to this study are included in this article.

Keywords

activated tungsten inert gas welding, distortions, residual stresses, SYSWELD, thermal cycles

Received: January 20, 2025

Revised: March 15, 2025

Published online:

- [1] C. Pandey, M. M. Mahapatra, P. Kumar, N. Saini, *J. Alloys Compd.* **2018**, *743*, 332.
[2] K. A. Venkata, S. Kumar, H. C. Dey, D. J. Smith, P. J. Bouchard, C. E. Truman, *Procedia Eng.* **2014**, *86*, 223.

- [3] B. Shanmugarajan, G. Padmanabham, H. Kumar, S. K. Albert, A. K. Bhaduri, *Sci. Technol. Weld. Joining* **2011**, *16*, 528.
[4] G. K. Padhy, V. Ramasubbu, N. Murugesan, C. Ramesh, S. K. Albert, *Sci. Technol. Weld. Joining* **2012**, *17*, 408.
[5] V. Bhanu, D. Fydrych, S. M. Pandey, A. Gupta, C. Pandey, *J. Mater. Eng. Perform.* **2023**, *33*, 12070.
[6] S. Suman, P. Biswas, S. Kumar, V. Pratap, A. Kumar, B. Kuriachen, *Mater. Today Proc.* **2020**, *21*, 1707.
[7] P. Nanavati, V. Bhedeka, S. Darshan, S. Darshan, I. Jaynish, C. Patel, M. Pandya, *Recent Advances in Mechanical Infrastructure. Lecture Notes in Intelligent Transportation and Infrastructure.*, Springer, Singapore **2021**.
[8] M. Vasudevan, *J. Mater. Eng. Perform.* **2017**, *26*, 1325.
[9] V. ArunKumar, M. Vasudevan, V. Maduraimuthu, V. Muthupandi, *Mater. Manuf. Process.* **2012**, *27*, 1171.
[10] V. Maduraimuthu, P. Vasantharaja, M. Vasudevan, B. S. Panigrahi, *J. Mater. Eng. Perform.* **2017**, *26*, 5938.
[11] M. Vasudevan, K. N. Gowtham, T. Jayakumar, *Int. J. Comput. Mater. Sci. Surf. Eng.* **2011**, *4*.
[12] A. Baksha, M. Vasudevan, *J. Mater. Eng. Perform.* **2013**, *22*, 3708.
[13] S. Nagaraju, P. Vasantharaja, N. Chandrasekhar, M. Vasudevan, T. Jayakumar, *Mater. Manuf. Process.* **2016**, *31*, 319.
[14] C. Pandey, N. Saini, M. M. Mahapatra, P. Kumar, *Int. J. Hydrogen Energy* **2016**, *41*, 17695.
[15] P. K. Taraphdar, R. Kumar, A. Giri, C. Pandey, M. M. Mahapatra, K. Sridhar, *J. Manuf. Process.* **2021**, *68*, 1405.
[16] C. Pandey, M. M. Mahapatra, P. Kumar, N. Saini, *Metall. Mater. Trans. B* **2018**, *49*, 2881.
[17] D. Deng, H. Murakawat, *Comput. Mater. Sci.* **2006**, *37*, 209.
[18] M. Zubairuddin, M. Vasudevan, P. V. Elumalai, M. Attar, P. R. Attar, E. Krishnasamy, *Int. J. Interact. Des. Manuf.* **2024**, <https://doi.org/10.1007/s12008-024-02138-w>.
[19] M. Zubairuddin, R. Ravi Kumar, B. Ali, *Optik* **2021**, *245*, 167510.
[20] M. Zubairuddin, S. K. Albert, M. S. Reddy, B. Ali, B. Varaprasad, A. Mishra, P. K. Das, P. V. Elumalai, *Mater. Today Proc.* **2023**, *72*, 1550.
[21] S. Kumar, R. Awasthi, C. S. Vishwanadham, K. Bhuanumurthy, G. K. Dey, *Mater. Des.* **2014**, *59*, 211.
[22] S. H. Kim, J. Kim, W. Lee, *J. Mater. Process. Technol.* **2005**, *167*, 480.
[23] A. Yaghi, T. Hyde, A. Becker, J. William, W. Sun, *J. Mater. Process. Technol.* **2009**, *209*, 3905.
[24] K. C. Ganesh, K. R. Balasubramanian, M. Vasudevan, P. Vasantharaja, N. Chandrasekhar, *Metall. Mater. Trans. B* **2016**, *47*, 1347.
[25] K. C. Ganesh, M. Vasudevan, K. R. Balasubramanian, P. Vasantharaja, N. Chandrasekhar, *Mater. Perform. Charact.* **2018**, *7*, 160.
[26] A. R. Pavan, B. Arivazhagan, M. Zubairuddin, S. Mahadevan, M. Vasudevan, *J. Mater. Eng. Perform.* **2019**, *28*, 4903.
[27] A. R. Pavan, N. Chandrasekar, B. Arivazhagan, S. Kumar, M. Vasudevan, *CIRP J. Manuf. Sci. Technol.* **2021**, *35*, 675.
[28] J. Goldak, A. Chakravati, M. Bibly, *Metall. Trans. B* **1984**, *15*, 299.
[29] C. Heinze, A. Pitter, M. Rethmeier, S. Babu, *Comput. Mater. Sci.* **2013**, *69*, 251.